

# Disappearance of the hexatic phase in a binary mixture of hard disks

John Russo\*

*School of Mathematics, University of Bristol, Bristol BS8 1TW, United Kingdom*

Nigel B. Wilding†

*Department of Physics, University of Bath, Bath BA2 7AY, United Kingdom*

(Dated: August 16, 2021)

Recent studies of melting in hard disks have confirmed the existence of a hexatic phase occurring in a narrow window of density which is separated from the isotropic liquid phase by a first-order transition, and from the solid phase by a continuous transition. However, little is known concerning the melting scenario in mixtures of hard disks. Here we employ specialized Monte Carlo simulations to elucidate the phase behavior of a system of large ( $l$ ) and small ( $s$ ) disks with diameter ratio  $\sigma_l/\sigma_s = 1.4$ . We find that as small disks are added to a system of large ones, the stability window of the hexatic phase shrinks progressively until the line of continuous transitions terminates at an end point beyond which melting becomes a first-order liquid-solid transition. This occurs at surprisingly low concentrations of the small disks,  $c \lesssim 1\%$ , emphasizing the fragility of the hexatic phase. We speculate that the change to the melting scenario is a consequence of strong fractionation effects, the nature of which we elucidate.

One of the most celebrated accomplishments of statistical mechanics is the progress in understanding the rich physics of phase transitions in two-dimensional (2D) systems. In particular, the melting of 2D crystals has puzzled researchers for decades. Early theoretical considerations [1] seemed to rule out the existence of 2D solids, while the celebrated *Mermin-Wagner* theorem [2, 3] proved rigorously that short-range continuous potentials cannot possess long-range positional order [4]. However, these theoretical ideas were in conflict with early simulation results for hard disks [5] which suggested the presence of a first-order phase transition between a liquid and a solid [5]. The early simulations established hard disks as a benchmark system for testing theories of 2D melting, and motivated [6] Kosterlitz and Thouless (KT) to develop the theory that now bears their name [7] (also independently found by Berezinskii [8]). Within the KT theory, a new type of 2D solid phase is proposed, having long-range orientational order and only quasi-long range positional order, and whose melting involves the continuous unbinding of dislocation pairs. The phase that results from the KT transition mechanism was originally believed to be an isotropic liquid, but Nelson, Halperin [9, 10], and Young [11], realized that the new phase retains quasi-long range orientational order, and melts via a second KT transition involving the unbinding of dislocations into free disclinations. The intermediate phase was called the *hexatic phase*, and the scenario of melting via two continuous transitions is known as the KTHNY theory.

The KTHNY theory is based on the assumption that the solid phase remains stable on decompression until the continuous dislocation unbinding transition. Consequently it does not rule out the possibility that this transition is pre-empted by a first-order transition, as simulations at first seemed to suggest. The two competing

scenarios were debated for decades see e.g. [12–16], until a new class of rejection-free algorithms was developed by Bernard and Krauth, called *event-chain* algorithms, that allowed the simulation of large systems in the melting region. This led to a surprising discovery [17]: the melting of hard disks occurs via a continuous KT transition between the solid and hexatic phase, and via a first-order transition between the hexatic and liquid phase. The work has been extended and generalized to soft potentials [18], to hard polygons [19], and to hard-sphere monolayers [20], where the findings were even verified experimentally for colloidal particles [21].

Hitherto, most studies of 2D melting have focused on pure systems. However, many important natural and technological systems are *mixtures* of different sized particles, and exhibit phase behaviour that is far richer and more complex than for pure systems. A specific question of fundamental interest is: “what happens to the melting transition of a system of pure hard disks when a low concentration of smaller hard disks is added?” This second species acts as a form of disorder which can selectively favor one particular phase, and might change the nature of the transition [22]. In this Letter we consider the melting scenario for such a binary system of hard disks. We choose the size ratio between large ( $l$ ) and small ( $s$ ) disks to be  $\sigma_l/\sigma_s = 1.4$ , which is large enough to constitute a significant perturbation, but small enough to ensure that the minority ( $s$ ) component is included substitutionally rather than interstitially in the solid phase. We define the concentration of small disks by  $c = N_s/(N_l + N_s)$ , with  $N_l$  and  $N_s$  the number of large and small disks respectively.

In order to correctly obtain accurate coexistence properties of mixtures, one needs to carefully account for fractionation effects ie. the different partitioning of species among the coexisting phases [24]. Open ensembles are

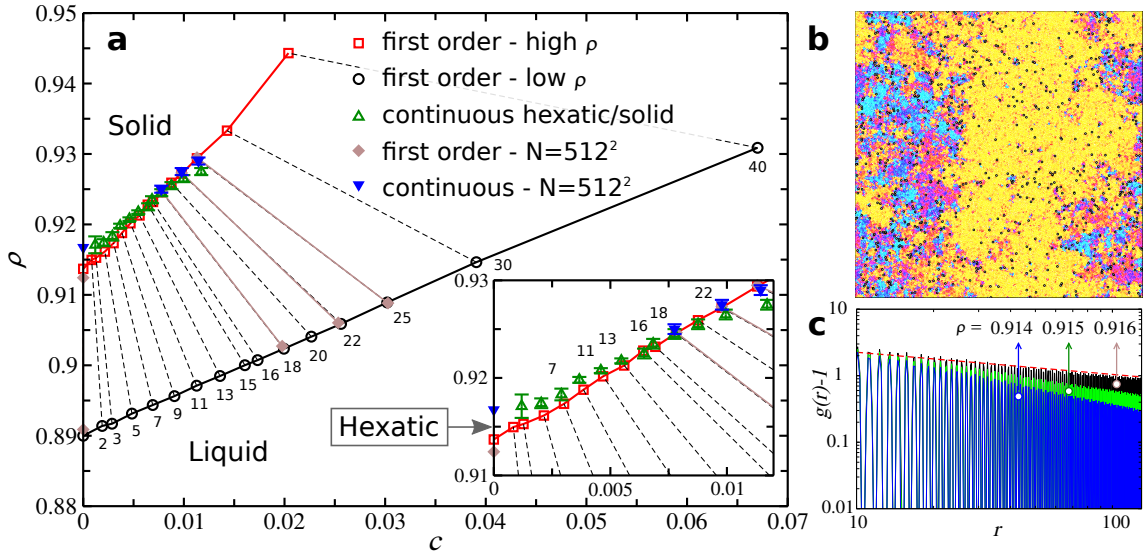


FIG. 1. **(a)** Phase diagram in the  $\rho$ - $c$  plane as discussed in the text. Dashed tie lines connect first-order coexistence points for various (marked) fugacity fractions ranging from  $\xi = 2$  to  $\xi = 40$ . Also shown is the line of continuous hexatic-solid transitions. Error bars were determined as described in the SM [23]. Data correspond to  $N = 256^2$  unless otherwise indicated. **(b)** Snapshot in the coexistence region at  $\xi = 15$  and  $\rho = 0.91$ . The color refers to the phase of the hexatic order parameter, while unfilled circles are small disks plotted for clarity with twice their true size. **(c)** Radial distribution function obtained by projecting the pair correlation function  $g(\Delta\mathbf{r})$  onto the direction of a lattice vector. Data is shown for  $\xi = 2$  at  $\rho = 0.914$  and  $0.915$  (hexatic phase), and  $\rho = 0.916$  (solid phase). The dashed line is the power-law scaling predicted by KTHNY theory.

particularly suited for this purpose as they permit global concentration fluctuations. Here we employ Monte Carlo (MC) simulation in the semi-grand canonical Monte ensemble (SGCE), in which a randomly selected disk can change its species [25] under the control of a fugacity fraction  $\xi = f_s/(f_l + f_s)$ , where  $f_s$  and  $f_l$  are the fugacities of the  $s$  and  $l$  disks respectively. The value of  $\xi$  sets the overall concentration which (due to fractionation) will generally differ from that of the individual phases. In order to accelerate local density and concentration fluctuations we implement the event-chain algorithm [17, 26], as well as a MC position swap for randomly selected pairs of disks. In the regime of small  $c$  of interest here,  $\xi$  is of the order of  $10^{-5}$  and for convenience we quote only its coefficient, e.g. we write  $\xi = 3$  instead of  $\xi = 3 \times 10^{-5}$ .

The hard disks occupy a periodic square box of side  $L$  which, in common with other lengths, we measure in units of  $\sigma_l$ . In order to study the effects on the phase behavior of varying  $c$ , we selected 16 different values of  $\xi$  in the interval  $\xi \in [0, 40]$ . For each  $\xi$ , we scanned (in a stepwise fashion) the range of number density  $\rho = (N_s + N_l)/L^2$  over which melting occurs. Within a two-phase region these paths of constant  $\xi$  correspond to *tie lines* along which phase separation occurs at constant fugacity for each component. We measured the pressure  $P$  along each tie line to obtain the corresponding equation of state (EOS),  $P(\rho)$ . This was found to exhibit the typical *van der Waals loop* of a first-order phase transition in a finite-sized system [27], which for pure hard disks corresponds to the liquid to hexatic tran-

sition [17]. Application of the Maxwell construction to the EOS permitted the determination of the coexisting densities that mark the termini of the tie line.

In order to locate the density of the KT transition separating the hexatic and solid phases, we extended to binary mixtures the methods introduced in Ref. [17]. Specifically, for each  $\xi$  we computed the form of the pair correlation function  $g(\Delta\mathbf{r})$  for a sequence of values of density. The hexatic-solid transition is signaled by a crossover in the form of  $g(\Delta\mathbf{r})$  from exponential (short-range, hexatic) order to power-law (quasi-long range, solid) behavior. Since 2D systems of disks can exhibit a very large correlation length, the accurate location of this crossover density requires simulations of considerable size and duration. Most of our estimates of phase behavior were performed, using  $N = N_s + N_l = 256^2$ , while  $N = 512^2$  was used for a selected number of fugacities in order to assess finite-size effects. Overall, our simulations consumed well over 100 years of single-core CPU time.

Fig. 1(a) presents our measurements of the density-concentration phase diagram. Apparent is a region of first-order phase coexistence delineated by coexistence state points connected by dashed tie lines. Within this region a lower density phase coexists with a higher density phase, the nature of which we now examine for a moderate value of  $\xi$ . A configurational snapshot inside the coexistence region at  $\xi = 15$  and  $\rho = 0.91$ , is displayed in Fig. 1(b) and shows small disks as unfilled circles, while large disks are colored according to the phase of the hexatic order parameter,  $\psi_6^j = \sum_k \exp(i6\theta_{jk})/n_j$ , where, for

each disk  $j, k$  is one of the  $n_j$  nearest neighbors (defined as the disks whose cells share one edge with  $j$  in the radial Voronoi tessellation of the plane), and  $\theta_{jk}$  is the angle that the vector  $r_{jk}$  makes with a reference direction. Evident is a strip of dense phase having strong hexatic ordering which is separated by a rough interface from a disordered (liquid) phase of lower density. The supplementary material (SM)[23] additionally shows that the EOS displays a van der Waals loop. Both these properties are the hallmarks of a first-order phase transition. Our phase diagram shows that on adding small particles, the region of first-order coexistence (as found for the pure system in Ref. [17]) extends along the concentration axis, moving to higher  $\rho$  (and higher  $P$ ). Interestingly, as  $\xi$  increases, the tie lines lengthen while their slope rapidly flattens, implying that small disks are more easily ‘dissolved’ in the disordered liquid phase. Our system thus behaves like a *eutectic mixture*.

Also indicated in Fig. 1(a) is the line of continuous hexatic-solid transitions, marked by the green and blue triangles, determined from the crossover in the form of the decay of the pair correlation function. The nature of this crossover [23] is shown in Fig. 1(c) which plots  $g(r) - 1$  for state points spanning the transition line. The blue curve exhibits exponential decay (albeit with a very long correlation length) characteristic of the hexatic phase, while the black curve exhibits power-law decay characteristic of the 2D solid. The power-law exponent is compatible with  $-1/3$  (red dashed line), which corresponds to the predicted stability limit of the solid phase within KTHNY theory. Our results show that, as small particles are added to the system, the continuous hexatic-solid transition point of the pure system becomes a line of KT transitions that extends to higher densities.

The inset of Fig. 1(a) expands the high density region of the phase diagram, revealing that as  $\xi$  is increased, the window of stability of the hexatic phase shrinks. For  $\xi = 20 \pm 2$ , corresponding to concentration  $c \approx 1\%$ , the KT line *intersects*—and extends metastably into—the region of first-order coexistence. Thereafter, for  $\xi \gtrsim 20$ , the liquid phase coexists with a solid rather than a hexatic phase. Such an intersection point is analogous to the critical end point that features in the phase diagrams of many binary mixtures [28, 29]. There a line of critical demixing transitions intersects and is truncated by a first-order transition line, the latter inheriting the singularities of the former. However, a difference between a critical end point and the end point in the present system is that the KT transition is a phase transition of infinite-order within the classification scheme of Ehrenfest, and thus the free energy and all its derivatives are continuous. Accordingly one expects that the first-order boundary in our system remains analytic.

In order to check for finite-size effects with regard to the phase behaviour, we performed simulations with  $N = 512^2$  for  $\xi = 0, 18, 22, 25$ , the results of which are

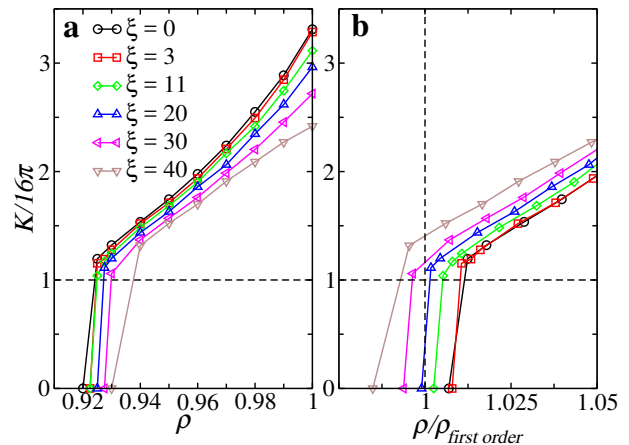


FIG. 2. **(a)** Normalized Young modulus ( $K/16\pi$ ) for various  $\xi$  as a function of  $\rho$ . The horizontal lines marks the stability limit  $K = 16\pi$  for the solid phase. **(b)** The same data plotted as a function of  $\rho/\rho_{\text{first order}}$ , the high density boundary of the first-order transition. The point with coordinates  $(\rho/\rho_{\text{first order}} = 1, K/16\pi = 1)$  marks the end point of the KT line (see text).

included in Fig. 1(a). As in Ref. [17], the first-order coexistence window for the pure system is observed to shrink noticeably with increasing system size, but this narrowing is much reduced at high  $\xi$  where the transition points are indistinguishable within our precision. The corresponding results for the KT line shift slightly to higher  $\rho$  with increased system size, but the results are still within the error bars. Overall, therefore, the  $N = 512^2$  results confirm the shrinking of the hexatic stability window.

Further evidence corroborating the disappearance of the hexatic phase with increasing  $\xi$  can be gleaned from a study of the elastic constants of the solid phase. More specifically, we exploit KTHNY predictions for the value of the Young’s modulus ( $K$ ) at the limit of stability of the solid phase, to independently deduce the locus of the KT line. Our approach follows Refs. [30, 31] and involves measurements of the Lagrangian strain tensor in combination with a finite-size scaling analysis [30] to yield estimates for the bulk and the effective shear moduli in the thermodynamic limit. Since this approach applies only to defect-free solids and is feasible only for much smaller system sizes than considered above, we implement it in SGCE MC simulations of  $N = 3120$  disks in which the generation of defects is suppressed by the simple expedient of rejecting any MC update that would create a dislocation pair of the smallest Burger’s vector. The resulting elastic constants provide an estimate of  $K$  for the constrained (ie. defect-free) solid, which we measure as a function of  $\rho$  for a number of values of  $\xi$ .

Of course, equilibrium configurations of an unconstrained solid actually contain a non-zero population of defects, and consequently the measurements of  $K$  must be corrected to take this into account. KTHNY the-

ory [10] provides a framework for doing so which involves solving a set of renormalization group recursion relations [31], starting from the  $K$  value of the defect-free configurations. The solution also requires an independent calculation of the fugacity of dislocation pairs  $y$ . As shown in Ref. [31], this quantity is proportional to the acceptance probability in the constrained ensemble simulations, which we match with the site-fraction  $N_i/N$  of dislocations pairs in the monodisperse system (see SM [23]). The corrected values of  $K$  for different values of  $\xi$  are plotted in Fig. 2(a). Note that KTHNY theory predicts the melting of the solid to occur when  $K/16\pi$  reaches unity under decompression, whereupon  $K$  jumps abruptly to zero. Fig. 2 thus shows that the effect of adding small disks is to increase the softness of the solid, i.e. lowering  $K$  with increasing  $\xi$ , and moving the KT transition density from  $\rho = 0.92$  for the pure case ( $\xi = 0$ ) to  $\rho = 0.935$  for  $\xi = 40$ .

Overall, the results emerging from Fig. 2(a) for the  $\xi$  dependence of the KT transition density are in good agreement with the results deduced from the pair correlation function that are shown in Fig. 1(a). Additionally, the data for  $K(\rho)$  confirms the disappearance of the hexatic phase. This can be appreciated by replotting  $K$  as a function of  $\rho/\rho_{\text{first order}}$ , with  $\rho_{\text{first order}}$  the high density boundary of the first-order transition at each value of  $\xi$ . Represented in this way, the data (Fig. 2(b)) reveal that the shift of the KT transition to higher density with increasing  $\xi$  is *slower* than the shift of the first-order boundary, which therefore ultimately engulfs it. The value of  $\xi$  for which the KT line reaches its endpoint can be read off from Fig. 2(b) by locating that curve which intersects the point whose coordinates are  $\rho/\rho_{\text{first order}} = 1$ ,  $K/16\pi = 1$ . Notwithstanding a certain sensitivity to the method by which the fugacity of dislocation pairs is determined, we estimate this to occur for  $\xi \cong 20$ , in accord with the previous estimate shown in Fig. 1(a).

We now attempt to rationalize the loss of the hexatic phase. To this end we search for changes in the structural character of the phases that might affect their entropy balance. We focus on three properties: (i) defect populations, (ii) spatial correlations between small particles, and (iii) degree of fractionation. Fig. 3(a) plots the density dependence of the population of those defects relevant for the KTHNY transition namely 5–7 dislocation pairs, free 5–7 dislocations and disclinations with 5 and 7 neighbors. Results are shown for  $\xi = 3$  (top panel) and for  $\xi = 30$  (bottom panel) [32]. Vertical dashed lines mark the coexistence boundary for the first-order transition, and for  $\xi = 3$  (top panel) the purple line marks the density of the continuous transition. One observes that the KTHNY sequence of dislocation pairs (solid)  $\rightarrow$  free dislocations (hexatic)  $\rightarrow$  free disclinations (liquid) is obeyed for all  $\xi$  considered. One also notes from Fig. 3(a) that on traversing the phase transitions, the site fraction ( $N_i/N$ ) of all topological defects remains practically un-

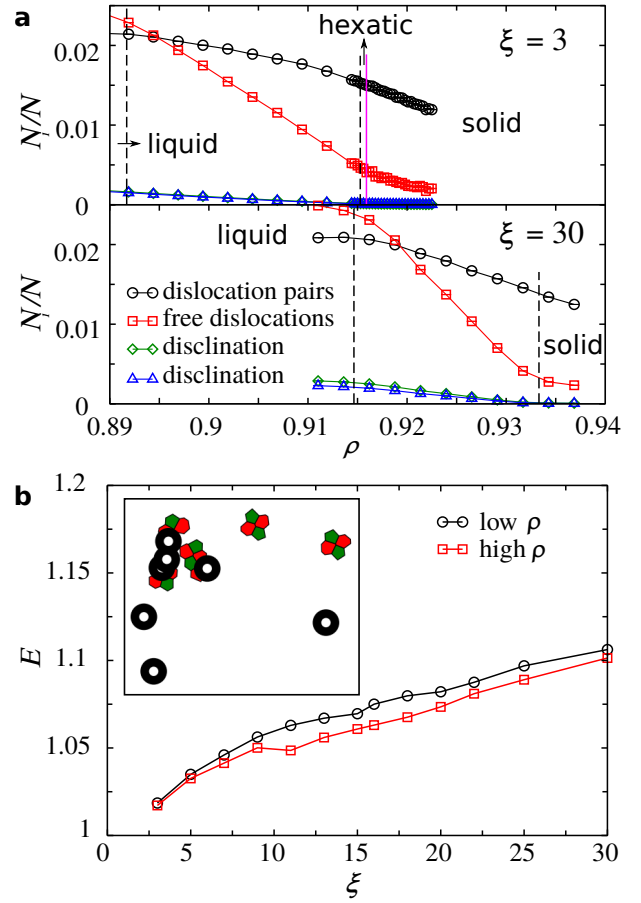


FIG. 3. (a) Fraction of sites with defects for  $\xi = 3$  (top panel) and  $\xi = 30$  (bottom panel). The dashed vertical lines represent the boundaries of the first-order phase transition. The vertical (purple) continuous line in the top panel marks the location of the continuous transition. (b)  $\xi$  dependence of the Pielou evenness index ( $E$ ) for state points at the low and high density boundary of the first-order coexistence region. The inset shows a snapshot for a small portion of a system at  $\xi = 30$  and  $\rho = 0.9343$ , where we plot both small disks (at twice their real size) and Voronoi cells representing topological defects with 5 (green cells) and 7 (red cells) neighbors. Large disks are omitted.

changed for both low and high  $\xi$  (a fact that is confirmed by the snapshots shown in Fig. S7 of the SM [23]).

In order to assess how small particles are distributed within the system, we plot in Fig. 3(b) their *Pielou* index ( $E$ ) as a function of  $\xi$  for densities on the low and high density boundary of the first-order coexistence region. This quantity measures the *evenness* of a distribution of points on a plane [33]:  $E = \pi \rho_s \bar{\omega}$ , where  $\rho_s$  is the number density of small disks and  $\bar{\omega}$  is the average squared distance between a randomly chosen point on the plane and the nearest small disk.  $E = 1$  signifies a random (Poisson) distribution, while  $E > 1$  indicates clustering. As Fig. 3(b) shows, the value of  $E$  in both the liquid and the high density phase grows strongly with increas-

ing  $\xi$ , indicating an increase in the clustering of small particles. Such clustering is confirmed visually by the snapshot shown in the inset of Fig. 3(b) which depicts a small area of the solid phase for  $\xi = 30$  (a larger portion is shown in Fig. S7 of the SM [23]). Interestingly, however, the  $E$ -index of the two phases are very similar for a given  $\xi$ , despite their very different values of  $c$  and degree of structural order. This latter finding suggests that the contribution of the clustering of small particles to the entropy of the solid and liquid phase are rather similar. We also note in passing that small particle clusters tend to occur together with clusters of defects as can be seen in the inset of Fig. 3(b), as well as Fig S7 of the SM [23])

Taken together, this evidence shows that (i) the addition of small particles seems to have negligible effects on the population of defects at the phase transitions; (ii) while the small particles cluster quite strongly at large  $\xi$ , there is little *difference* in the degree of small particle clustering between the phases (which might otherwise alter their entropy balance). Accordingly, it is not clear that one can attribute the loss of the hexatic to either changes in defect populations or to particle clustering. Instead we speculate that the effect is primarily driven simply by fractionation. Specifically, as  $\xi$  increases, the small particles show a strong preference to migrate to the liquid phase. This in turn raises the (mixing) entropy of the liquid much more than it does that of the hexatic or the solid phase. The result is to stabilize the liquid relative to the higher density phase and hence to shift the first-order coexistence region to higher density faster than the KT line. Ultimately, then, the liquid region engulfs the hexatic, leaving only liquid-solid coexistence in its stead.

To conclude, using tailored large-scale MC simulations, we have investigated the melting scenario of a binary mixture of hard disks with  $\sigma_l/\sigma_s = 1.4$  as a function of the fugacity fraction  $\xi$  of the small particles. We have shown that the hexatic phase that occurs in the pure case survives only for very low concentrations of small particles  $c \lesssim 1\%$ , demonstrating that it is an utmost delicate state of matter. For larger  $c$  the melting scenario changes into a first-order transition between the liquid and solid phases, a finding which we have argued is a corollary of the stabilizing effect of strong fractionation of small particles to the liquid phase.

**Acknowledgments** We thank H. Tanaka and R. Evans for helpful discussions. JR thanks the Royal Society for a URF fellowship, and the Blue Crystal supercomputer at the University of Bristol for a generous allocation of resources. Part of this research made use of the Balena High Performance Computing Service at the University of Bath.

- 
- \* john.russo@bristol.ac.uk  
† n.b.wilding@bath.ac.uk
- [1] R. Peierls, *Helv. Phys. Acta* **7**, 158 (1934).
  - [2] N. D. Mermin and H. Wagner, *Phys. Rev. Lett.* **17**, 1133 (1966).
  - [3] N. D. Mermin, *Phys. Rev.* **176**, 250 (1968).
  - [4] P. Hohenberg, *Phys. Rev.* **158**, 383 (1967).
  - [5] B. Alder and T. Wainwright, *Phys. Rev.* **127**, 359 (1962).
  - [6] J. M. Kosterlitz, *Rep. Prog. Phys.* **79**, 026001 (2016).
  - [7] J. Kosterlitz and D. Thouless, *J. Phys. C* **5**, L124 (1972).
  - [8] V. Berezinskii, *Sov. Phys. JETP* **32**, 493 (1971).
  - [9] B. Halperin and D. R. Nelson, *Phys. Rev. Lett.* **41**, 121 (1978).
  - [10] D. R. Nelson and B. Halperin, *Phys. Rev. B* **19**, 2457 (1979).
  - [11] A. Young, *Phys. Rev. B* **19**, 1855 (1979).
  - [12] K. J. Strandburg, *Rev. Mod. Phys.* **60**, 161 (1988).
  - [13] H. Weber, D. Marx, and K. Binder, *Phys. Rev. B* **51**, 14636 (1995).
  - [14] J. Dash, *Rev. Mod. Phys.* **71**, 1737 (1999).
  - [15] A. Jaster, *Phys. Rev. E* **59**, 2594 (1999).
  - [16] C. Mak, *Phys. Rev. E* **73**, 065104 (2006).
  - [17] E. P. Bernard and W. Krauth, *Phys. Rev. Lett.* **107**, 155704 (2011).
  - [18] S. C. Kapfer and W. Krauth, *Phys. Rev. Lett.* **114**, 035702 (2015).
  - [19] J. A. Anderson, J. Antonaglia, J. A. Millan, M. Engel, and S. C. Glotzer, *Phys. Rev. X* **7**, 021001 (2017).
  - [20] W. Qi, A. P. Gantapara, and M. Dijkstra, *Soft Matter* **10**, 5449 (2014).
  - [21] A. L. Thorneywork, J. L. Abbott, D. G. Aarts, and R. P. Dullens, *Phys. Rev. Lett.* **118**, 158001 (2017).
  - [22] J. T. Kindt, *J. Chem. Phys.* **143**, 124109 (2015).
  - [23] J. Russo and N. Wilding, Supplementary material provides details of the determination of: a) the first order and KT lines; b) fractionation effects; c) elastic constant.
  - [24] N. B. Wilding and P. Sollich, *J. Chem. Phys.* **133**, 224102 (2010).
  - [25] D. Frenkel and B. Smit, *Understanding Molecular Simulation*, Vol. 1 (Academic press, 2001).
  - [26] M. Michel, S. C. Kapfer, and W. Krauth, *J. Chem. Phys.* **140**, 054116 (2014).
  - [27] K. Binder, B. J. Block, P. Virnau, and A. Tröster, *American Journal of Physics* **80**, 1099 (2012).
  - [28] M. E. Fisher and P. J. Upton, *Phys. Rev. Lett.* **65**, 2402 (1990).
  - [29] N. B. Wilding, *Phys. Rev. Lett.* **78**, 1488 (1997).
  - [30] S. Sengupta, P. Nielaba, M. Rao, and K. Binder, *Phys. Rev. E* **61**, 1072 (2000).
  - [31] S. Sengupta, P. Nielaba, and K. Binder, *Phys. Rev. E* **61**, 6294 (2000).
  - [32] We consider only dislocation pairs of the smallest Burger's vector, as these are the most abundant at the densities considered.
  - [33] E. C. Pielou, *J. Theor. Biol.* **13**, 131 (1966).



## Supplementary Information for “Disappearance of the hexatic phase in a binary mixture of hard disks”

### FIRST-ORDER TRANSITION: VAN DER WAALS LOOP

In mean field theories of first-order phase transitions, a so-called van der Waals (vdW) loop refer to the parts of the equation of state (EOS),  $P(\rho)$ , that are mechanically unstable. Beyond mean field theory the situation is more subtle, particularly for simulation. There a phenomenon akin to the vdW loop occurs (and which therefore retains the name), but it has a very different origin. Specifically the vdW loop observed in simulations arises from interfacial effects [27], theoretical analysis of which predicts that in the limit of large  $N$  the area under the loop scales as the interfacial free energy per disk,  $\delta f \propto N^{-1/2}$ . An example of such a vdW loop for our system is given in Fig. S4, showing the pressure ( $\beta P\sigma_l^2$ ) as a function of the specific volume  $v = 1/\rho$  for simulations at  $\xi = 2$ . The symbols are results from simulations, while the continuous red line is a high-order polynomial fit to the simulation data. The standard Maxwell construction (dashed line) is used to obtain the coexistence densities, while the area under the Maxwell construction defines the interface free energy cost of forming an interface,  $\beta\Delta f$ . We test the expected scaling in Fig. S5 where we compare the vdW loop for  $\xi = 22$  at three different system sizes,  $N = 512^2$  (circles),  $N = 256^2$  (squares), and  $N = 128^2$  (diamonds). As shown in the inset of Fig. S5, the scaling is indeed compatible with  $\beta\Delta f \propto N^{1/2}$  despite the relative softness of the interface for first-order coexistence in hard disks implying that it is difficult to reach the scaling limit in this system.

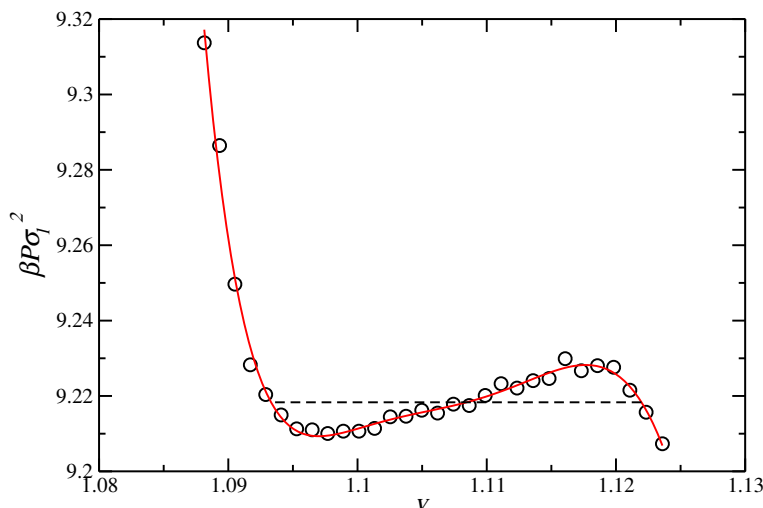


Fig. S4. Equation of state for  $\xi = 2$ . Symbols are results from SGCE simulations, the continuous red line is a high-order polynomial fit, while the dashed line is the Maxwell construction.

In Fig. S6 we compare the EOS for a large range of  $\xi$ . With increasing  $\xi$  one observes two features: firstly that the coexistence region shifts to higher densities  $\rho$ , and pressures  $\beta P\sigma_l^2$ , and secondly that the free energy barrier between the two phases (which is proportional to the area under the Maxwell construction) grows steadily. This latter feature reflects the increasing difficulty of nucleating the dense phase from the liquid as the concentration of small disks increases towards the eutectic point; it is at the origin of the glass-forming ability of the mixture near the eutectic point.

### CONTINUOUS TRANSITION: PAIR CORRELATION FUNCTIONS

To locate the continuous transition, we scan for each  $\xi$  a sequence of densities  $\rho$ . The sequence commences at the high density boundary of the first-order transition and increases in steps of  $\Delta\rho = 0.0005$  until the solid phase is reached. For each density considered, we perform 10 independent simulation runs, each of which yields a measurement

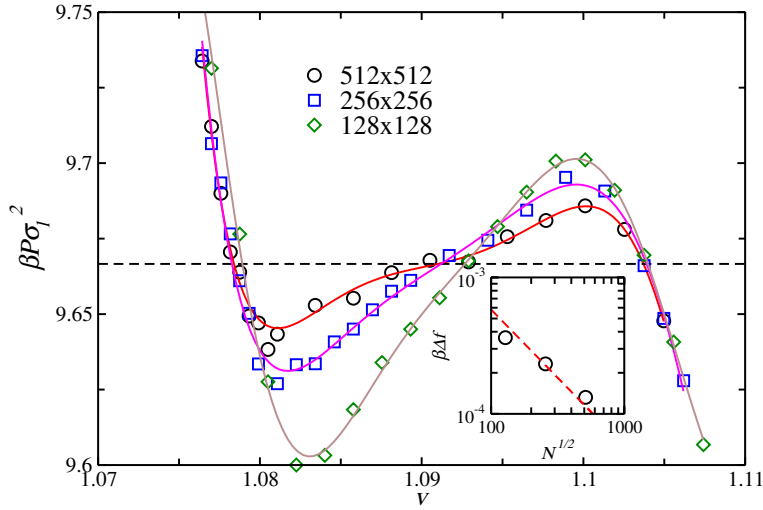


Fig. S5. Equation of state for  $\xi = 22$  for three system sizes. Continuous lines are high-order polynomial fits, while the dashed line is the Maxwell construction for the largest system. The inset shows that the scaling of the interface energy for each disk  $\beta\Delta f$ , with the dashed line representing  $\beta\Delta f \propto N^{1/2}$ .

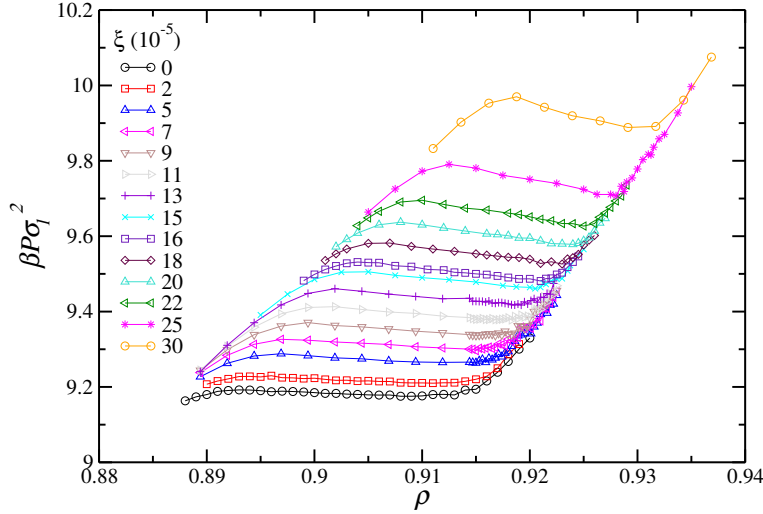


Fig. S6. Equation of state for different  $\xi$ .

of the pair correlation function  $g(\Delta\mathbf{r})$ . We estimate the density of the continuous transition by finding the crossover in the form of  $g(\Delta\mathbf{r})$  from exponential (short-range, hexatic) to power-law (quasi-long range, solid) behavior.

The continuous transition is intrinsically smeared out in a finite-sized system. This is manifest in the fact that even for a state point that is exactly at the transition density, separate independent simulation runs may yield differing forms of the decay of  $g(\Delta\mathbf{r})$ . An example is shown in Fig. S7 which displays two independent measurements of the pair correlation function for  $\xi = 11$  and  $\rho = 0.9207$ , obtained by performing a one dimensional projection of the full two-dimensional pair correlation,  $g(\Delta\mathbf{r})$ , onto the direction of a lattice vector. The black curve shows the result of a run which yielded exponential decay, albeit with a very long correlation length, while the red curve shows the result of a run which yielded power-law decay in the accessible window. The power-law exponent is compatible with  $-1/3$  (green dashed line in the figure), which corresponds to the stability limit of the solid phase in KTHNY theory.

Given this phenomenology, we estimate the location of the continuous transition for a given  $\xi$  by determining that density for which half of the associated 10 independent trajectories exhibit a pair correlation function  $g(r)$  with a power-law decay (while the rest give exponential decay). The error bars on the transition density in Fig. 1(c) in the main text are determined as follows: the lower-bound indicates the state point at which less than 20% of the 10 independent runs yield power-law decay of  $g(r)$ , while the upper bound indicates the state point at which at least

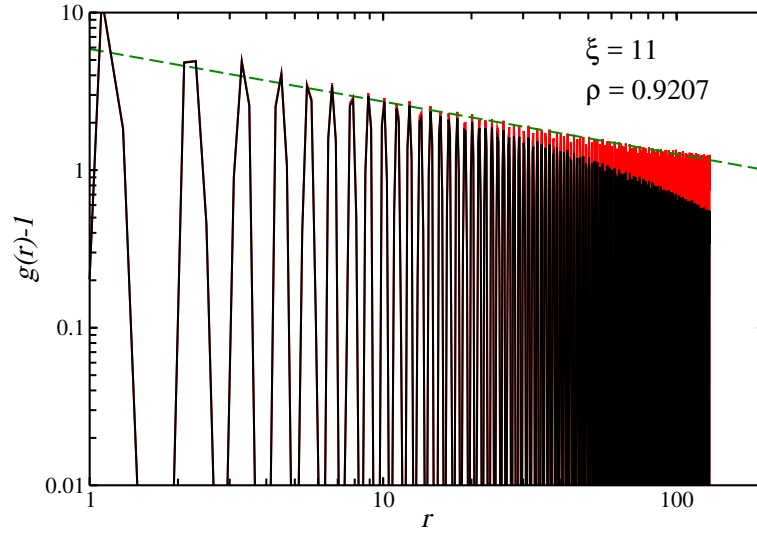


Fig. S7. The pair correlation function computed for two independent runs at  $\xi = 11$  and  $\rho = 0.9207$ : black line for the hexatic phase, red line for the solid phase, green dashed line is the power-law scaling predicted by KTHNY theory. The system size is  $N = 256^2$ .

80% of the trajectories have power-law decay.

Fig. S8 illustrates how the pair correlation function (as measured for our largest system size,  $N = 512^2$ ) varies as one crosses the transition density at fixed  $\xi = 22$ . Data are shown for two densities that straddle the continuous transition, and an intermediate density at the transition point.

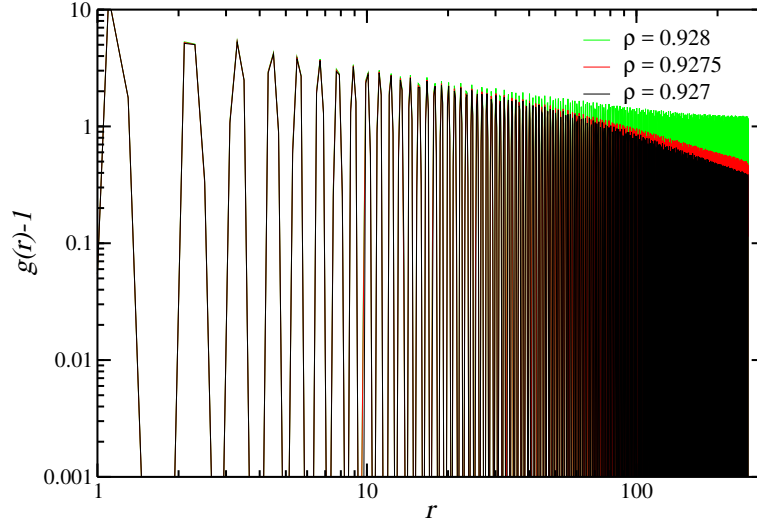


Fig. S8. The pair correlation function for three densities covering the continuous transition at  $\xi = 22$ . The system size is  $N = 512^2$ .

## FRACTIONATION

Fig. S9 provides further information on the fractionation of small disks between the different phases. It plots the  $\rho$  dependence of the concentration  $c$  for different fixed values of  $\xi$ . Dashed lines mark the coexistence line of the first-order transition, while open symbols give the location of the continuous transition. The results confirm the large difference in  $c$  between the fluid and the hexatic phases seen in fig 1a of the main text, and shows that there is a much smaller difference between the hexatic and solid phases.



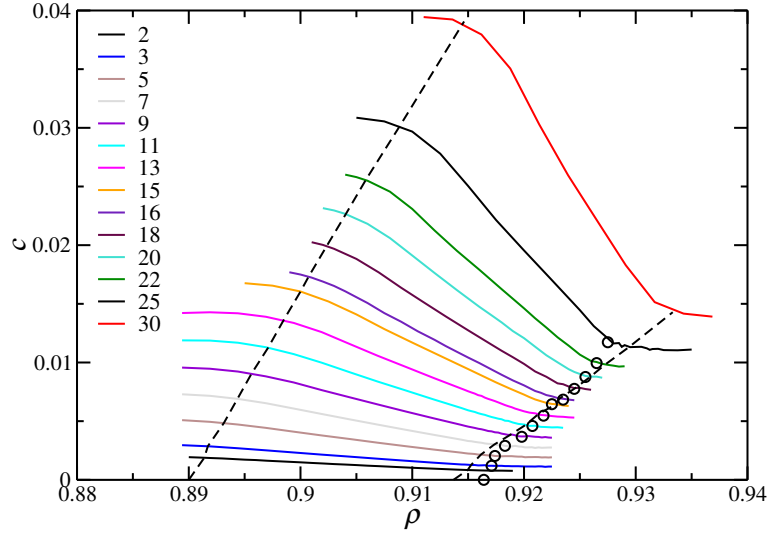


Fig. S9.  $\rho$  dependence of the concentration  $c$  of small disks, for different  $\xi$  (continuous lines). Dashed lines represent the coexistence lines of the first-order transition, while open symbols indicate the location of the continuous transition.

It is illuminating to visualize the configurations of small particles, particularly in relation to other structural features such as solid phase defects. The snapshots in Fig. S10(a) and (b) show examples of the distribution of small disks for  $\xi = 3$  and  $\xi = 30$  respectively at densities corresponding to the stability limit of the solid phase. The plots (which for clarity display only a quarter of the full  $N = 256^2$  particle system) confirm that  $c$  is much larger for  $\xi = 30$  than for  $\xi = 3$ . They also reveal (as noted in the main text) that the small particles are much more clustered for  $\xi = 30$  and furthermore there is a high correlation between these small particle clusters and the location of clustered topological defects, i.e. grain boundaries.

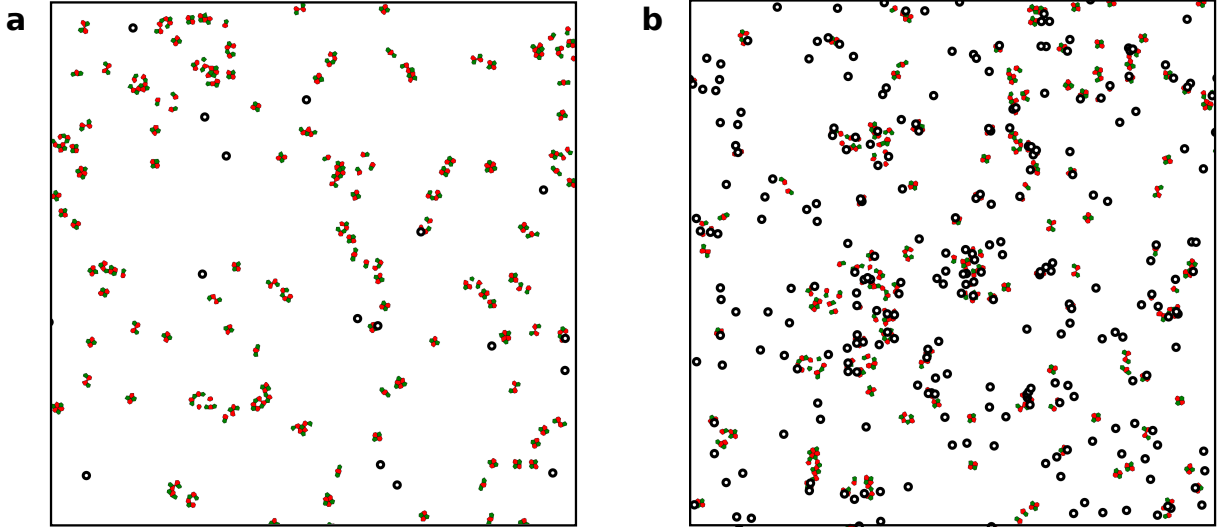


Fig. S10. (a) Configurational snapshots of a sub-volume of the  $N = 256^2$  system size for  $\xi = 3$ ,  $\rho = 0.9171$ . Small disks are shown at twice their real size (large disks are omitted). Also shown are the Voronoi cells representing topological defects with 5 (green cells) and 7 (red cells) neighbors. (b) As for (a) but for  $\xi = 30$ ,  $\rho = 0.9343$ .

As explained in the main text, the Pielou index ( $E$ ) quantifies the degree of clustering of the small disks. In Fig. S11 we plot this index for a wide range of values of  $\xi$ . Each curve corresponds to a different  $\xi$ , and the corresponding coexistence densities are marked with full symbols on the curve, and by a dashed line connecting these symbols. Following one curve from low to high density, the  $E$  index increases rapidly on entering the coexistence region, before attaining a maximum having  $E > 1$  in the middle of this region. This peak reflects the combined effects of

fractionation and phase separation: the preference of the small disks for the liquid phase artificially enhances the  $E$ -index when the liquid phase has a fractional volume  $< 1$  i.e. when it occupies a sub-volume of the system. Beyond the middle of the coexistence region, the artificial enhancement of  $E$  diminishes in tandem with the fractional volume of the liquid phase. On reaching the high density boundary of the coexistence region,  $E$  continues to decrease, until on entering the solid region its  $\rho$ -dependence flattens out. For each  $\xi$ , the  $E$  index of the two coexisting densities (full symbols) is almost the same, as discussed in the main text. This implies that the first-order transition involves two phases that, despite their very different  $c$ , have the same evenness, as discussed in the main text.

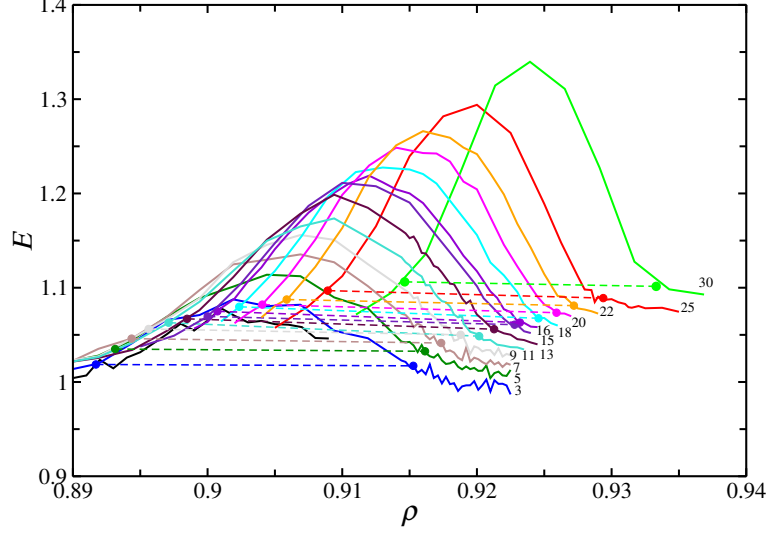


Fig. S11. Density dependence of the Pielou evenness index for various fugacities ranging from  $\xi = 2$  (bottom curve) to  $\xi = 30$  (top curve). The full symbols on each curve mark the coexisting densities of the first-order transformation, while the dashed line represents the coexistence region.

### COMPUTATION OF THE ELASTIC CONSTANTS

Here we outline the procedure for the calculation of the elastic constants. For a more in-depth discussion we refer the reader to Refs. [30, 31].

The first step involves the calculation of the elastic constants of a defect-free triangular solid of  $N = 3120$  disks in a quasi-square box. The most probable topological defect is the formation of a dislocation pair of the smallest Burger's vector, where a configuration of four disks having 7-5-7-5 neighbors appears. This can be avoided by rejecting all Monte Carlo moves which result in a disk having a number of neighbors different from 6. Neighbors are defined by constructing the Delaunay triangulation which is dual to the Voronoi tessellation of the plane. In this restricted ensemble, the linearized stress tensor can be computed

$$\epsilon_{ij} = \frac{1}{2} \left( \frac{\partial u_i}{\partial R_j} + \frac{\partial u_j}{\partial R_i} \right),$$

where  $i, j$  refer to the components  $x$  and  $y$  of a Cartesian coordinate system in the body reference frame (Lagrangian representation of the stress tensor),  $u_i$  is the displacement vector between the position of a disk and its reference lattice position, and  $R_i$  is the lattice vector corresponding to that disk. Fluctuation in the stress tensor define the compliance matrix

$$S_{ijkl} = \langle \epsilon_{ij} \epsilon_{kl} \rangle.$$

For the calculation of the elastic constants the relevant components of the compliance matrix are  $S_{11} = \langle \epsilon_{xx} \epsilon_{xx} \rangle$  and  $S_{12} = \langle \epsilon_{xx} \epsilon_{yy} \rangle$ . From these, one can build the linear combinations  $S_{++} = 2(S_{11} + S_{12})$  and  $S_{--} = 2(S_{11} - S_{12})$ , and

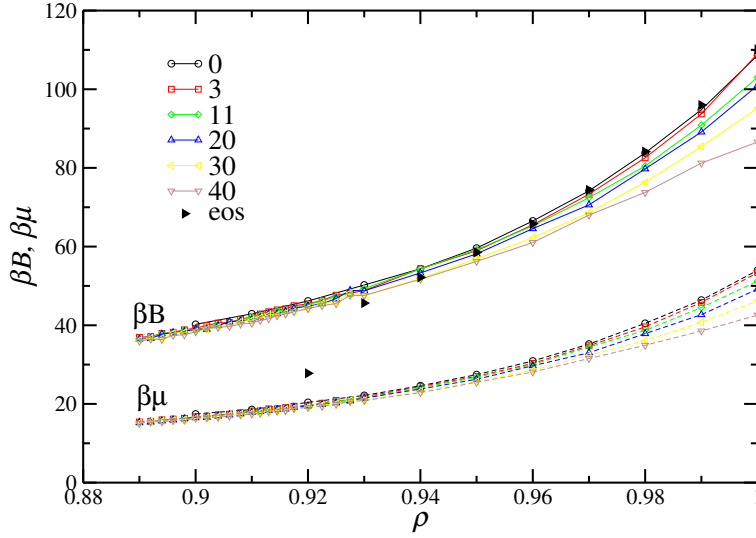


Fig. S12. Bulk ( $B$ ) and effective shear ( $\mu$ ) modulus as a function of density  $\rho$ , for various values of the fugacity fraction  $\xi$  (symbols). The full symbols plot the bulk modulus computed from the equation of state of the unconstrained system.

obtain the bulk ( $B$ ) and effective shear modulus ( $\mu$ ) as

$$\beta B = \frac{1}{2S_{++}} ,$$

$$\beta \mu = \frac{1}{2S_{--}} .$$

The system size independent values of  $S_{++}$  and  $S_{--}$  are obtained via finite-size scaling. For each simulation of size  $L$ , we measure the fluctuations of the strain tensor in sub-boxes of size  $L_b$ . The  $L_b/L$  dependence of these fluctuations can be computed via a quadratic Landau functional. Fitting simulation results with the appropriate functional form [30] allows the determination of the size independent fluctuations  $S_{++}$  and  $S_{--}$ . In our case, the fluctuations at system size  $L_b$  are obtained by averaging over 100 sub-boxes randomly placed within the system, and over 10 independent runs. The fitting procedure is then applied for system sizes  $L_b/L < 0.5$ , which gave the best agreement with the values of the bulk modulus independently computed via the equation of state (see below).

To compute the elastic constants of mixtures, the calculations above are run in the SGCE ensemble, where small disks substitutionally occupy a lattice position of the solid, and swap moves allow for fast sampling of independent configurations. To check for ensemble-dependence, we have run the same calculations also in the NVT ensemble, with the concentration of small disks fixed at the equilibrium values, and observed no difference in the results.

Fig. S12 plots the bulk ( $B$ ) and effective shear ( $\mu$ ) modulus for the monodisperse case ( $\xi = 0$ ) and for mixtures with fugacity fraction ( $\xi$ ). As a consistency check we can compare the results of the bulk modulus for the monodisperse system (open black circles), with an independent estimate of the bulk modulus via the following relation

$$B = \rho \frac{\partial P}{\partial \rho} .$$

The corresponding bulk modulus, computed with independent unconstrained simulations, is plotted in Fig. S12 with full triangle symbols. We observe that, at high  $\rho$ , there is excellent agreement between the bulk modulus computed via the strain tensor (open circles) and the one computed from the equation of state (full symbols). This agreement breaks down at low  $\rho$ , because of crystalline defects that proliferate in the unconstrained simulations, and eventually cause the crystal to melt.

With the values of  $B$  and  $\mu$  of Fig. S12 we can obtain the Lamé' coefficient  $\lambda = B - \mu$ , and from this compute the Young elastic modulus  $K$

$$K = \frac{8}{\sqrt{3}\rho} \frac{\mu}{1 + \mu/(\lambda + \mu)} .$$

In order to apply the KTHNY recursion relations, we need an estimate of the fugacity of dislocation pairs,  $y = \exp(-E_c)$ , defined in terms of the core energy of the dislocation,  $E_c$ . We can obtain this from the dislocation pair

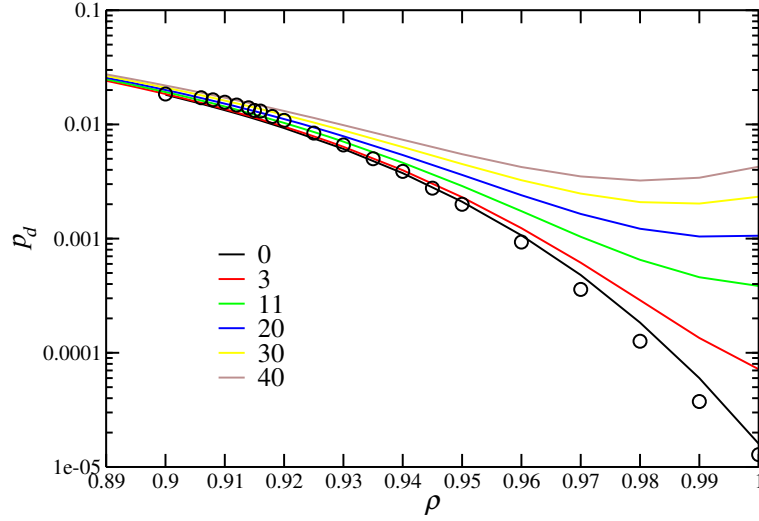


Fig. S13. Probability of dislocation pairs  $p_d$  for different values of  $\xi$  (continuous lines). The open symbols plot the site-probability  $N_i/N$  of finding a lattice site in a dislocation pair.

probability ( $p_d$ ) via the following relation

$$p_d = \exp(-2E_c) \frac{2\pi\sqrt{3}}{K/8\pi - 1} I_0 \left( \frac{K}{8\pi} \right) \exp \left( \frac{K}{8\pi} \right), \quad (1)$$

where  $I_0$  is a Bessel function.

Following Ref. [31], we can assume that  $p_d$  is proportional to the acceptance probability of the constrained MC simulations that conserve the topology of the Delaunay triangulation. To fix the proportionality constant, for the monodisperse case, we compute the site probability  $N_i/N$  of finding a dislocation pair in unconstrained simulations, and compare it to the acceptance probability of constrained MC simulations. This is shown in Fig. S13 where we plot the  $\rho$  dependence of the site probability  $N_i/N$  for the monodisperse case (open black symbols), and the acceptance probability of the constrained MC simulations after a simple rescaling (continuous black line). We can see that the two quantities have a very similar density dependence. We then compute  $p_d$  from the acceptance rate of constrained simulations of binary mixtures, and observe that  $p_d$  increases with increasing  $\xi$  (continuous lines in Fig. S13). At high fugacity fraction ( $\xi \gtrsim 20$ ) we observe that  $p_d$  is a non-monotonous function of  $\rho$ , and starts increasing at high values of  $\rho$ . This is due to the re-entrant melting of the solid phase at high density, which is typical of eutectic systems below the eutectic point.

From the values of  $p_d$  in Fig. S13, we use Eq. 1 above to extract  $E_c$ , and finally  $y$ .

The KTHNY recursion relations give the renormalized value of the Young modulus ( $K$ ) and the fugacity of dislocations ( $y$ ) in the limit  $l \rightarrow \infty$

$$\begin{aligned} \frac{\partial K^{-1}}{\partial l} &= 3\pi y^2 \exp(K/8\pi) \left[ \frac{1}{2} I_0 \left( \frac{K}{8\pi} \right) - \frac{1}{4} I_1 \left( \frac{K}{8\pi} \right) \right], \\ \frac{\partial y}{\partial l} &= \left( 2 - \frac{K}{8\pi} \right) y + 2\pi y^2 \exp(K/16\pi) I_0 \left( \frac{K}{8\pi} \right), \end{aligned}$$

which are solved with a Runge-Kutta scheme with  $\Delta l = 0.001$  until  $l = 100$ .

At the transition, the values of  $K$  jump discontinuously to zero. The transition points computed through KTHNY theory are plotted as square symbols in Fig. S14. The figure also plots the location of the first-order (circle symbols) and continuous transitions (diamond symbols) obtained with MC simulations. Both calculations predict the shrinking of the hexatic phase stability window, and a melting transition that is first-order at high  $\xi$ .

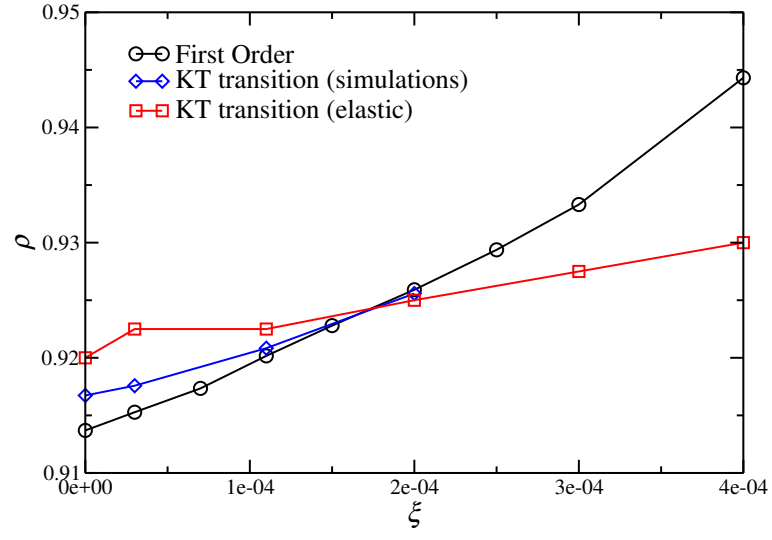


Fig. S14. Transitions points as a function of  $\xi$ . Circle symbols represent the  $\rho$  of the first-order transition points (the high- $\rho$  branch); diamonds symbols mark the location of the continuous transition estimated with MC simulations; squares symbols mark the continuous transition estimated with KTHNY theory after calculation of the elastic constants.